Bol. Soc. Paran. Mat.
©SPM – E-ISSN-2175-1188
SPM: www.spm.uem.br/bspm

(3s.) **v. 2026 (44) 2** : 1–24.
ISSN-0037-8712
doi:10.5269/bspm.78793

Entropy Generation and Heat Transfer Analysis in Triangular Solar Stills Using TiO_2 Nanofluid Flow with the Darcy-Brinkman Forchheimer and Ree-Eyring Model

Hamayat Ullah, Muhammad Salim Khan, Zahir Shah*, Aseel Smerat, and Maria Alina Fălădău

Abstract: This research focused on entropy generation in the triangular solar still based on a nanofluid of TiO_2 under the influences of magnetohydrodynamics (MHD), double-diffusive convection, and the Darcy-Brinkman-Forchheimer and Ree-Eyring models. The non-dimensional forms of the governing equations were solved by means of the Galerkin Finite Element Method (FEM) using COMSOL Multiphysics. The analysis of the major parameters with regard to flow, temperature distribution, entropy generation, and their combined effect on heat transfer has been supported with comparative sketches and tables, all validated by grid independence tests to assure computational accuracy. It is found that the flow circulation and hence convective heat transfer increased with increasing values of the Ree-Eyring parameter . It was also found that for high values of the Ree-Eyring parameters η, the nature of heat transfer progressively changed and became conduction dominant beyond a certain value. Increased Darcy numbers (Da) promote a flow towards convection-dominance in heat transfer processes by allowing a more superior permeability of flow and local Nusselt number. Increased porosity ϵ reduces resistance and on the other hand strengthens convection and temperature uniformity with a graph where the local Nusselt number is taken down to a lower level because of reduced effective thermal conductivity. Magnetic effects (Ha) suppress convection but bring about a considerable increase of 100% in the magnetic entropy generation while reducing the viscous entropy generation by25.77%. These will provide very good guidance in model optimization of nanofluid based solar stills, following the interrelationship of MHD, fluid dynamics, and thermal efficiencies of sustainable energy systems.

Key Words: Entropy generation, double-diffusive convection, triangular solar still, TiO_2-nanofluid, Galerkin Finite Element Method (FEM).

Contents

* Corresponding author.
2020 *Mathematics Subject Classification:* 76W05, 76S05.
Submitted September 06, 2025. Published January 21, 2026

Symbol/Name	Description
B_0	Intensity of magnetic field
P	Dimensionless pressure
d_m	Diameter of cylinder (m)
Pr	Prandtl number
C_p	Heat capacitance
Ra	Rayleigh number
Da	Darcy number
S_{Local}	Dimensionless entropy generation
Fc	Forchheimer coefficient
T	Temperature (K)
g	Gravitational acceleration (m/s^2)
T_h	Hot part temperature (K)
Ha	Hartmann number
T_c	Cold part temperature (K)
k	Thermal conductivity (W/mK)
u, v	Velocity components (m/s)
K	Permeability
U, V	Nondimensional velocity components
Nu_{avg}	Average Nusselt number
x, y	Coordinates (m)
Nu_{Local}	Local Nusselt number
X, Y	Dimensions
p	Pressure (N/m^2)
η	Ree-Eyring parameter
Greek symbols	
α	Thermal diffusivity (m^2/s)
ν	Kinematic viscosity (m^2/s)
β	Thermal expansion coefficient (1/K)
ρ	Density (kg/m^3)
ϵ	Porosity
σ	Electrical conductivity (1/m)
θ	Dimensionless temperature
ψ	Non-dimensional stream function
ϕ	Volume fraction
ω	Rotational speed (m/s)
μ	Dynamic viscosity (kg/ms)
Subscripts:	
avg	Average
nf	Nanofluid
bf	Basefluid
loc	Local
T_c	Cold temperature
np	Nanoparticles
T_h	Hot temperature

1. Introduction

A number of studies have been carried out on performance, design enhancement, and optimization of the solar stills in order to maximize freshwater production. Ghachem et al. [1] carried out numerical analysis, three-dimensional free convection of a double diffusion little to a solar distiller with focus on entropy generation. Their effort resulted in the fact that the system's loss of irreversibility could be

greatly minimized through optimal management of heat and mass transfer. Developing this further, Ghachem et al. [2] examined the joint effects of natural convection and radiation heat transfer in a three-dimensional solar thermal collector and the need to maximize the efficiency of heat transfer by variations in inclination angle. Later on, when Ghachem et al. [3] researched the effect of resting on inclined solar distillers, even more optimization work showed that a geometric orientation would help to improve both the heat and mass transfer performance. Previous studies on transient behavior had been conducted by Dhiman [4], who investigated the temporal performance of a sphere-based solar still and gave significant evidence regarding the thermal response pattern of the still. Also, the evaporation efficiency of the modified geometry was higher than that of the traditional planar surfaces since a concave wick evaporation surface was studied by Kabeel [5]. Ismail [6] designed a portable hemispherical solar still and claimed to have better portability and usefulness without affecting performance. Arunkumar et al. [7] used experimental research to test a hemispherical solar still and examine how improved capture of incident radiation resulted in a significant jump in freshwater yield. Equally, Gorjian et al. [8] conducted experiments on a stand-alone point-focus parabolic solar collector and yielded a high degree of productivity due to the collection of heat via focusing. Tiwari and Kumar [9] screened the possibility of nocturnal water production in tubular solar stills with waste heat used to preheat brine, wherein residual waste heat could be utilized successfully to drive the system through the night. Amimul et al. [10] developed an enhanced solar still, whose construction was tested, indicating a measurable increase in thermal efficiency and the amount of resulting distillate due to better design characteristics. Other innovations of the past few years include different geometries and hybridization methods to enhance the effectiveness of solar stills. Elashmawy [11] conducted an experiment with an experimental parabolic concentrator system fitted with a solar tracking system mounted on a tubular solar still and tested it to reveal that a sun tracking system and its concentrated radiation boosted by a very large margin the production of the distillate. In an experimental study, Taamneh and Taamneh [12] explored the pyramid-shaped solar stills and found increased productivity as a result of multi-faceted incident incidence. Fatha et al. [13] evaluated pyramid-shaped and single-slope stills based on thermal-economic considerations and found that the former geometry promised better thermo-economic characteristics, combined with 20 percent higher energy efficiency and cheaper cost per unit of water produced. Kianifar et al. [14] have also studied pyramid-shaped systems in terms of exergy and economics which revealed that active systems were superior to passive systems in both their performances and economics. Investigation has been devoted to design improvements to pyramid stills. To improve the solar capture, Arunkumar et al. [15] introduced a boosting mirror that can result in an improved thermo-physical performance and distillate yield. Kabeel et al. [16] tested hollow circular fins and phase change materials (PCMs) on pyramid-shaped stills and were able to achieve increased productivity with a more stable night time operation. On the same note, Sathyamurthy et al. [17] revealed the ability of PCMs to outstandingly supplement freshwater generation through thermal energy storage so as to allow evaporation at night. Sathyamurthy et al. [18] described performance influencing factors of the triangular pyramid solar stills and singled out the geometric design, properties of kind of materials and operating parameters as being of key determinants. Nagarajan et al. [19] developed a forced cover cooling make-up of triangular pyramid stills, which also led to higher condensation rates and total yield. Nevertheless, Sathyamurthy et al. [20] demonstrated that PCMs used in triangular pyramid models to improve maintaining the heat level and making the evaporation process last longer resulted in increased overall daily yield. A triangular pyramid solar still coupled with an inclined still that had baffles was theoretically investigated by Naveen Kumar et al. [21] to demonstrate that the hybrid reduced evaporation-condensation cycles and raised the distillate yield. Almeshaal et al. [22] investigated the 3D natural convection L-shaped enclosure filled with MWCNT-nanofluids under the consideration of nanoparticle aggregation in a Rayleigh-B Enberg system and observed that the aspect of aggregation had a crucial, immensely joking advantage as far as heat exchange is concerned in this setup. According to Hussain et al. [23], MHD mixed convection of Al; O; 3 -Cu-water hybrid nanofluid in a wavy channel containing a fixed cylinder showed that the magnetic field strength indicator and the nanoparticle intensity had a significant impact on thermal performance. Hadji and et. Al. in collaboration has worked a great deal in the modelling of functionally graded (FG) nanostructures. They recently suggested a quasi-3D theory of higher shear deformation to vibrations of an FG carbon nanotube reinforced composite beam on an elastic foundation

to enhance higher accuracy of prediction to the item in [24]. Analytical free vibration solution of FG nanoplates has been obtained in [25], whereas [26] suggested a nonlocal free vibration analysis of porous FG nanobeams by hyperbolic shear deformation theory. Khelifa et al. [27] investigated the buckling behavior of compound beams reinforced by CNTs in presence of a stretching effect which brought to light the contribution of CNTs volume fraction and foundation stiffness. Stability and thermal conductivity of nanofluids Nanofluids Nanofluids made up of water and carbon nanotubes were also analyzed by Farboda et al. [28] in terms of their flow stability and discovered that dispersion stability plays a very important role in their continued thermal performance. Kabeel et al. [29] theoretically and experimentally proved a modified solar still using nanofluids and outward condenser, which guarantees higher productivity because of better heat absorption and condensation capability. Sharshir et al. [30] did a study on which had a glass cover cooling nanofluid enhancement in experimentally measured solar stills, demonstrating significant performance boosts due to a combination of improved conductivity and faster condensation. Based on an experimental study, Kabeel et al. [31] investigated the depth of water on the performance of a pyramid solar still with a new absorber plate coated with TiO 2 nano black paint. It was discovered that a lower depth of water led to a considerable increase in the rate of evaporation and amount of distillate yielded because of more rapid increase of temperature and because of increased thermal absorption. Al-Rashed et al. [32] performed a study concerning the impact of the magnetic field inclination on magneto-convective irreversibilities in a CNT-water nanofluid-filled cubic cavity to see that the magnetic field direction has a significant effect on entropy generation rate as well as heat transport patterns. Xue [33] provided a theoretical framework of the effective thermal conductivity of carbon nanotube composite, showing that the aspect ratio, orientation of CNTs, and good quality of dispersion of the tubes are important to achieve a maximum thermal enhancement. Rahman et al. [34] numerically investigated the double diffusive natural convection in a triangular solar collector and demonstrated that the coupling of solutal and thermal buoyancy forces causes the effect of heat and mass transfer efficiency, whose geometric configuration has a major contribution in the process of performance optimization.

This research distinguishes itself through several novel contributions that advance the understanding of heat transfer in complex systems. First, it explores the application of TiO_2-H_2O nanoliquid in a fluid-saturated porous medium, offering potential enhancements in thermal performance. In addition, it synthesizes the Ree-Eyring model with an imposed external horizontal magnetic field, enabling a deeper examination of magnetohydrodynamic effects on flow and thermal patterning phenomena. The study further incorporates the Darcy-Forchheimer model to characterize momentum within the porous medium, marking the first time this approach has been employed in the specific geometry under consideration. Moreover, a detailed analysis of entropy generation is performed in this rare geometric configuration, offering new insights into thermal performance optimization and system efficiency.

Building on these unique aspects, the study aims to address several key research questions. It investigates how the use of TiO_2-H_2O nanoliquid can improve heat transfer efficiency in porous media saturated with fluids. It also examines the influence of coupling the Ree-Eyring model with an externally applied horizontal magnetic field on both flow and thermal patterns. Furthermore, the study evaluates how incorporating the Darcy-Forchheimer model enhances the representation of momentum in this particular geometric configuration. Another important focus is on identifying the role of entropy generation in this geometry and its contributions to the thermal performance and overall efficacy of the system. Finally, the research explores how primary thermophysical and geometric parameters affect the average Nusselt number, total entropy generation, and Bejan number within the system.

2. Studied Configuration

The present study focuses on the investigation of natural convection heat transfer in a triangular enclosure filled with a nanofluid and a fluid-saturated porous medium, subjected to varying thermal boundary conditions. The base wall is uniformly heated to a higher temperature (T_h), while the inclined side walls are maintained at a lower temperature (T_c), resulting in a buoyancy-driven flow due to the imposed temperature gradient. This configuration can be linked to solar desalination systems, where solar energy passes through the transparent cover of a solar still, generating temperature gradients that drive heat flux. These heat fluxes cause evaporation of saline water and subsequent condensation of pure vapor, yielding fresh water. The porous medium introduces resistance to fluid motion and enhances thermal

dispersion, while the use of nanofluid improves thermal conductivity, thereby increasing heat transfer efficiency. An externally applied uniform magnetic field (B_0), oriented parallel to one of the cold walls, is incorporated to study its influence on the flow and thermal characteristics. The introduction of the magnetic field is motivated by its potential to control and optimize heat and mass transfer in electrically conducting fluids. In practical applications, such as in magnetohydrodynamic (MHD) power systems, solar desalination units containing conducting nanofluids, and cooling of electronic devices, applying an external magnetic field is feasible through the use of permanent magnets or electromagnets positioned near the enclosure. This provides an effective means to suppress or regulate convective motion via the Lorentz force, which can be beneficial in reducing thermal losses or controlling flow instability. The scope of this research includes analyzing the combined effects of the porous medium, nanofluid thermophysical properties, and magnetic field on the temperature distribution, heat transfer performance, and system efficiency. The physical configuration and relevant boundary conditions are illustrated in **Fig. 1**, where all necessary elements including the heated base wall, cooled inclined walls, porous medium, nanofluid region, magnetic field direction, and flow circulation are clearly labeled to facilitate understanding of the setup.

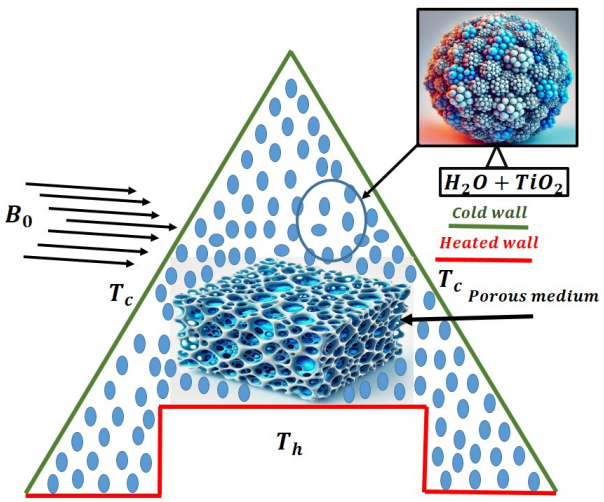

Fig. *1*. Physical sketch illustrating the flow dynamics in the system studied.

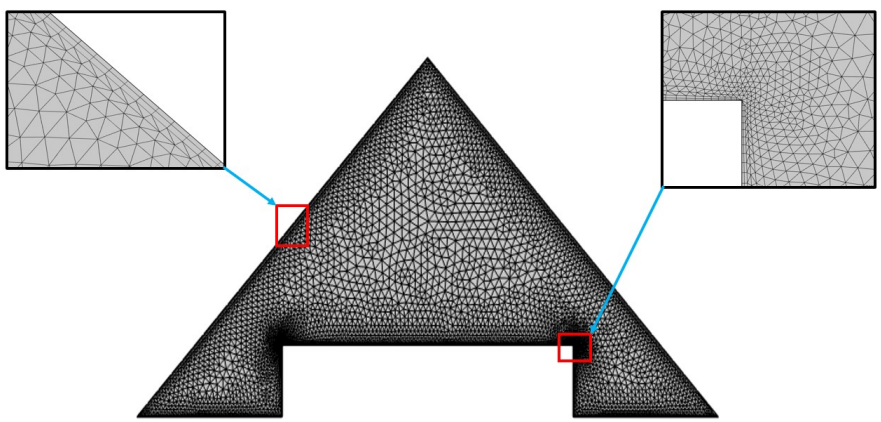

Fig. 2. Grid distribution at extra fine meshing level.

2.1. Mathematical formulation

The governing equations for fluid flow in porous media can be derived using the Darcy-Brinkmann-Forchheimer generalized equation, which integrates momentum conservation under porous conditions, as outlined in reference [35]:

$$\frac{\partial u}{\partial x} + \frac{\partial v}{\partial y} = 0, \tag{2.1}$$

$$\frac{1}{\epsilon^2}\left(u\frac{\partial u}{\partial x}+v\frac{\partial u}{\partial y}\right)=-\frac{1}{\rho_{nf}}\frac{\partial P}{\partial x}+\frac{\nu_{nf}}{\epsilon}(1+\frac{1}{\beta c})\left(\frac{\partial^2 u}{\partial x^2}+\frac{\partial^2 u}{\partial y^2}\right)-\frac{\nu_{nf}}{K}u-\frac{F_c}{\sqrt{K}}u|u|, \tag{2.2}$$

$$\frac{1}{\epsilon^2}\left(u\frac{\partial v}{\partial x}+v\frac{\partial v}{\partial y}\right)=-\frac{1}{\rho_{nf}}\frac{\partial P}{\partial y}+\frac{\nu_{nf}}{\epsilon}(1+\frac{1}{\beta c})\left(\frac{\partial^2 v}{\partial x^2}+\frac{\partial^2 v}{\partial y^2}\right)-\frac{\nu_{nf}}{K}v-\frac{F_c}{\sqrt{K}}v\,|u|+\beta_{nf}g\,(T-T_{avg})-\frac{\sigma_{nf}}{\rho_{nf}}B_0^2 v, \tag{2.3}$$

$$(\rho c_p)_{nf}\left(u\frac{\partial T}{\partial x}+v\frac{\partial T}{\partial y}\right)=k_{nf}\left(\frac{\partial^2 T}{\partial x^2}+\frac{\partial^2 T}{\partial y^2}\right). \tag{2.4}$$

The velocity magnitude is given by the expression $|\mathrm{u}|=\sqrt{u^2+v^2}$. The Forchheimer coefficient, F_c, is defined as $F_c=\frac{b}{\sqrt{a}\epsilon^{\frac{3}{2}}}$, where a=150 and b=1.75. This coefficient characterizes the effective thermal conductivity within a nanofluid-saturated porous medium. In this context, K denotes the permeability of the porous structure, while ε signifies the porosity. These definitions are in line with the theoretical frameworks presented in references [36][37].

$$K=\frac{\epsilon^3 d_m^2}{150(1-\epsilon)^2}, \tag{2.5}$$

$$\left.\begin{array}{l} u=v=0, T=T_h, \\ u=v=1, T=T_c, \\ u=v=0, \frac{\partial T}{\partial n}=0. \end{array}\right\} \tag{2.6}$$

$$X=\frac{x}{L},\quad Y=\frac{y}{L},\quad U=\frac{uL}{\alpha_{bf}},\quad V=\frac{vL}{\alpha_{bf}},\quad \theta=\frac{T-T_f}{T_h-T_f},\quad P=\frac{(p+\rho_{bf}gy)\,L^2}{\rho_{\mathrm{bf}}\alpha_{bf}^2}, \tag{2.7}$$

$$\eta=\frac{1}{\beta c},\ Ra=\frac{\beta_{bf}g(T_h-T_f)L^3}{\alpha_{bf}\nu_{bf}},\quad Ha=LB_0\sqrt{\frac{\sigma_{bf}}{\mu_{bf}}},\quad Da=\frac{K}{L^2},\quad Pr=\frac{\nu_{bf}}{\alpha_{bf}}. \tag{2.8}$$

In accordance with the previously stated assumptions, the governing equations are formulated in Eq. (2.1) to Eq. (2.5) and subsequently rendered in their non-dimensional form as follows:

$$\frac{\partial U}{\partial X}+\frac{\partial V}{\partial Y}=0, \tag{2.9}$$

$$\frac{1}{\epsilon^2}\frac{\rho_{nf}}{\rho_{bf}}\left(U\frac{\partial U}{\partial X}+V\frac{\partial U}{\partial Y}\right)=-\frac{\partial P}{\partial X}+\frac{1}{\epsilon}\frac{\nu_{nf}}{\nu_{bf}}\mathrm{Pr}(1+\frac{1}{\eta})\left(\frac{\partial^2 U}{\partial X^2}+\frac{\partial^2 U}{\partial Y^2}\right)-\frac{\nu_{nf}}{\nu_{bf}}\frac{\mathrm{Pr}}{Da}-\frac{F_c}{\sqrt{Da}}|u|U, \tag{2.10}$$

$$\frac{1}{\epsilon^2}\left(U\frac{\partial V}{\partial X}+V\frac{\partial V}{\partial Y}\right)=-\frac{\partial P}{\partial Y}+\frac{1}{\epsilon}\frac{\nu_{nf}}{\nu_{bf}}\mathrm{Pr}(1+\frac{1}{\eta})\left(\frac{\partial^2 V}{\partial X^2}+\frac{\partial^2 V}{\partial Y^2}\right)-\frac{\nu_{nf}}{\nu_{bf}}\frac{\mathrm{Pr}}{Da}V-\frac{F_c}{\sqrt{Da}}|u|\,V+\frac{\beta_{\mathrm{nf}}}{\beta_{\mathrm{f}}}\mathrm{Pr}\cdot Ra\theta+\frac{\sigma_{\mathrm{f}}}{\rho_{nf}}\frac{\rho_{\mathrm{f}}}{\rho_{\mathrm{nf}}}\frac{\mathrm{Pr}}{\epsilon}\frac{Ha^2}{\sqrt{Ra}}V, \tag{2.11}$$

$$U\frac{\partial\theta}{\partial X}+V\frac{\partial\theta}{\partial Y}=\frac{\alpha_{nf}}{\alpha_{bf}}\left(\frac{\partial^2\theta}{\partial X^2}+\frac{\partial^2\theta}{\partial Y^2}\right). \tag{2.12}$$

3. Entropy Generation

A generalized non-dimensional expression for local entropy generation, accounting for these effects, was formulated by Woods [38] and is given as:

$$S_{Local}=\frac{k_{hnf}}{k_{bf}}\left(\left(\frac{\partial\theta}{\partial X}\right)^2+\left(\frac{\partial\theta}{\partial Y}\right)^2\right)+\chi\frac{\mu_{nf}}{\mu_{bf}}\left\{(U^2+V^2)+Da\left[2\left(\frac{\partial U}{\partial X}\right)^2+2\left(\frac{\partial V}{\partial Y}\right)^2+\left(\frac{\partial U}{\partial Y}+\frac{\partial V}{\partial X}\right)^2\right]\right\}+\frac{\rho_{nf}}{\rho_f}\chi Ha^2V^2, \tag{3.1}$$

$$S_{Local}=S_{Thermal}+S_{Viscous}+S_{Magnetic} \tag{3.2}$$

$$S_{Thermal}=\frac{K_{nf}}{k_{bf}}\left(\left(\frac{\partial\theta}{\partial X}\right)^2+\left(\frac{\partial\theta}{\partial Y}\right)^2\right), \tag{3.3}$$

$$S_{Viscous} = \chi \frac{\mu_{nf}}{\mu_{bf}} \left\{ \left(U^2 + V^2\right) + Da \left[2\left(\frac{\partial U}{\partial X}\right)^2 + 2\left(\frac{\partial V}{\partial Y}\right)^2 + \left(\frac{\partial U}{\partial Y} + \frac{\partial V}{\partial X}\right)^2 \right] \right\}, \tag{3.4}$$

$$S_{Magnetic} = \frac{\rho_{nf}}{\rho_f} \chi Ha^2 V^2, \tag{3.5}$$

$$\chi = \frac{\mu_{nf} T_{avg}}{k_{bf} K} \left(\frac{\alpha_{bf}}{L\left(T_h - T_c\right)} \right)^2, \quad T_{avg} = \frac{T_h + T_c}{2}$$

Here, χ denotes the irreversibility distribution ratio, which quantifies the relative contribution of heat transfer irreversibility to total entropy generation. In the present study, χ is assigned a fixed value of 10^{-5}. The entropy generation rate is formulated as follows:

$$S_{Total} = \frac{1}{V} \iint S_{Local} dV. \tag{3.6}$$

Where V represents the **total control volume** occupied by the nanofluid within the computational domain.

4. Nusselt Number and Related Parameters

The Nusselt number is a dimensionless parameter that characterizes the efficiency of convective heat transfer relative to conductive heat transfer. The local Nusselt number (Nu_{Local}) quantifies the heat transfer rate at a specific point on the surface, depending on local flow velocity, temperature gradients, and geometric features. The average Nusselt number (Nu_{avg}) provides a global measure of thermal performance by integrating Nu_{loc} over the entire heated surface. In this study, Nu_{Local} and Nu_{avg} are evaluated in the presence of key governing parameters: the Ree–Eyring parameter (η), Darcy number (Da), Hartmann number (Ha), and porosity (ϵ). These parameters influence the Nusselt number by altering fluid flow patterns, thermal boundary layer thickness, and the conduction–convection balance. Specifically, η modifies fluid rheology and shear-thinning effects, Da controls permeability and convective strength in porous media, Ha regulates magnetohydrodynamic effects on flow stability, and ϵ impacts flow resistance and heat distribution. Understanding the coupled influence of these parameters on Nu_{Local} and Nu_{avg} enables targeted optimization of heat transfer in the desalination process. The formulation for the local and average Nusselt number are defined as [39]:

$$Nu_{Local} = -\left(\frac{k_{nf}}{k_{bf}}\right) \frac{\partial \theta}{\partial X}, \tag{4.1}$$

$$Nu_{avg} = \int_0^L Nu_{Local}\, dY. \tag{4.2}$$

5. Evaluation of Nanofluid Thermophysical Properties

Accurate assessment of nanofluid thermophysical properties density (ρ), specific heat (Cp),thermal conductivity (k), thermal expansion (β), and electrical conductivity (σ) is critical for predicting heat and mass transfer in thermal systems. The thermophysical properties of the base fluid (water) and nanoparticles are summarized in Table 1. The effective density, thermal conductivity, and specific heat capacity of the nanofluid are mathematically expressed as follows:

$$\rho_{nf} = (1-\phi)\rho_{bf} + \phi\rho_{Tio_2}, \tag{5.1}$$

$$(\beta\rho)_{nf} = (1-\phi)(\beta\rho)_{bf} + \phi(\beta\rho)_{Tio_2}, \tag{5.2}$$

$$(\rho c_p)_{nf} = (1-\phi)(\rho c_p)_{bf} + \phi(\rho c_p)_{Tio_2}, \tag{5.3}$$

The thermophysical properties of the TiO_2–water nanofluid were evaluated using widely accepted mixture models. The effective thermal conductivity was determined using the *Maxwell–Garnett* model [40], which accounts for the effect of dispersed spherical nanoparticles on the base fluid conductivity:

$$k_{nf} = k_{bf} \left[\frac{k_{Tio_2} + 2k_{bf} - 2\phi(k_{bf} - k_{Tio_2})}{k_{Tio_2} + 2k_{bf} + \phi(k_{bf} - k_{Tio_2})} \right], \tag{5.4}$$

The **electrical conductivity** of the nanofluid was modeled using the *Hamilton–Crosser* formulation [41]:

$$\sigma_{nf}=\sigma_{bf}\left[1+\frac{\left(\frac{\sigma_{Tio_2}}{\sigma_{bf}}-1\right)\phi}{\left(\frac{\sigma_{Tio_2}}{\sigma_{bf}}+2\right)-\left(\frac{\sigma_{Tio_2}}{\sigma_{bf}}-1\right)\phi}\right], \tag{5.5}$$

The **dynamic viscosity** was estimated using the *Einstein* model for dilute suspensions [42]:

$$\mu_{nf}=\mu_{bf}(1-\phi)^{-2.5}. \tag{5.6}$$

Table *1.* Thermophysical properties of water and nanoparticles *[36].*

Property	Water (H_2O)	Titanium Dioxide (TiO_2)
ρ	997.1	4250
C_p	4179	686.2
k	0.613	8.9538
β	$21\times\ 10^{-5}$	$0.9\times\ 10^{-5}$
σ	0.05	$1\times\ 10^{-12}$

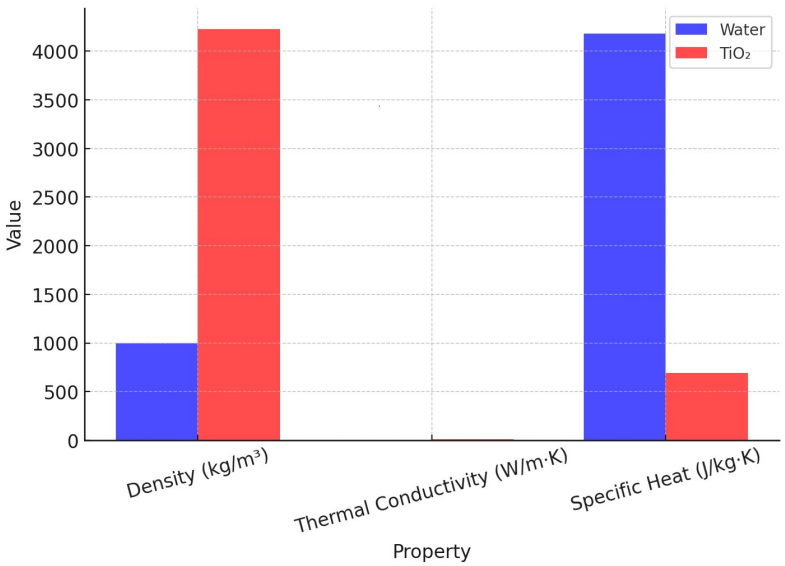

Fig. *3.* Thermophysical properties of water and nanoparticles.

Table *2.* The computed average Nusselt number values corresponding to different levels of mesh refinement are presented.

Refinement Level	**D.O.F**	**NEL**	$\boldsymbol{Nu_{average}}$
Normal	12200	1345	12.928
Fine	17842	2043	13.536
Finer	26606	3169	14.077
Extra Fine	**68718**	**8519**	**16.175**
Extremely Fine	174306	22415	17.957

6. Method of Solution and Code Validation

We solved dimensionless governing equations (9-12), including their associated boundary conditions, using COMSOL Multiphysics 6.0, a finite element method (FEM)-based software. The domain of the computational problem was subdivided into several components, in which velocity, pressure, and temperature parameters were evaluated by taking suitable approximation functions for each domain. The task geometry was constructed and input values and parameters were filled up with applied boundary conditions.

Convergence was compared with the following criterion judged on the relative error occurring over the iterations:

$$\left| \frac{\Gamma^{n+1} - \Gamma^{n}}{\Gamma^{n}} \right| < \varepsilon \tag{6.1}$$

where (n) is iteration number, (Γ) incorporates all variables such as temperature, pressure and velocity components (u, v)and (ϵ) is convergence threshold. For the purpose of this study, the convergence criterion was considered at ($\epsilon = 10^{-6}$). The Grid distribution at extra fine meshing level. **Fig. 2.** Schematic flow chart of computational scheme show in **Fig.** 4.

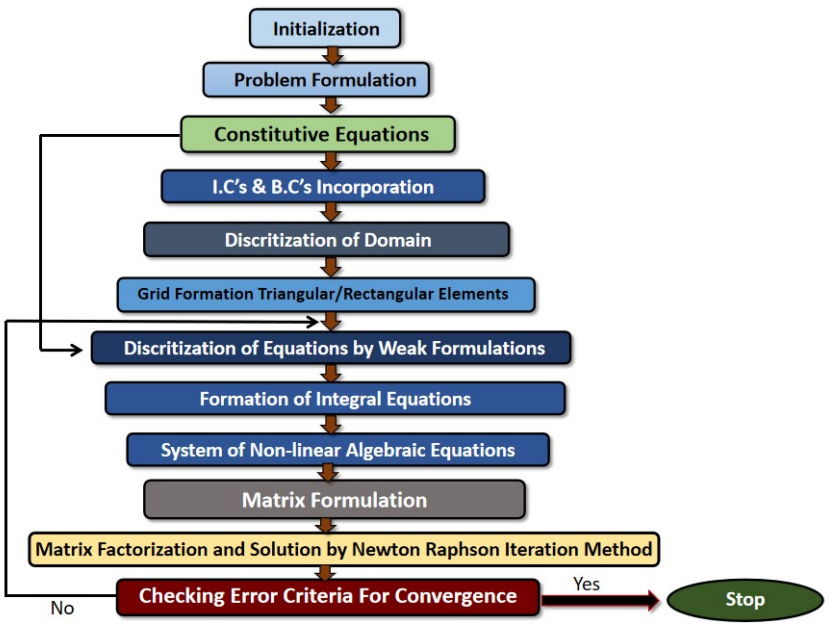

Fig. 4. Schematic flow chart of computational scheme.

6.1. Grid sensitivity test

The reliability and accuracy of finite element method (FEM) simulations are highly dependent on the attainment of grid independence. This is established through a grid independence test, which ensures that the numerical solution exhibits negligible sensitivity to further mesh refinement. As illustrated in Table 1, the average Nusselt number converges and exhibits minimal variation between refinement levels 8 and 9 (R.L-8 and R.L-9), under fixed conditions of (Pr = 0.71, AR = 0.50, Sc = 10^{-2}, Ra = 10^{5}). This convergence behavior validates the adequacy of refinement level 8 for subsequent simulations, striking an optimal balance between computational efficiency and solution accuracy as shown in Table 2. The Comparison of average Nusselt number $\mathrm{Nu_{Avg}}$ against (Ha) with published data are shown in Fig. 5, Fig. 6 and in Table 3.

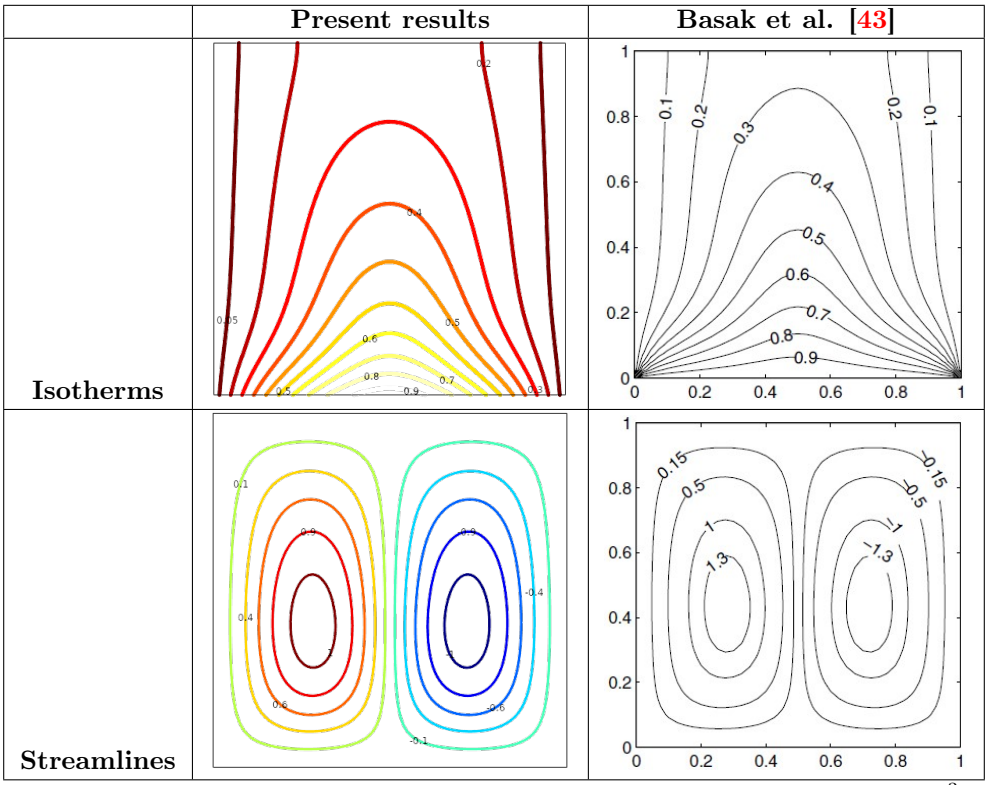

Fig. *5*. Graphical comparison, $\theta(X,0) = 1$ with Ha=0, $Pr = 7.0$, $Ra = 5 \times 10^3$.

Table *3*. Comparison of average Nusselt number Nu_{Avg} against (Ha).

S.no	**Ha**	$\boldsymbol{Nu_{Avg}}$ **in Present work**	$\boldsymbol{Nu_{Avg}}$ **in** [44]
1	0	7.6082	7.578
2	20	6.7246	6.910
3	40	5.5178	5.873
4	60	4.8546	5.175
5	80	4.6286	4.801
6	100	4.5603	4.627

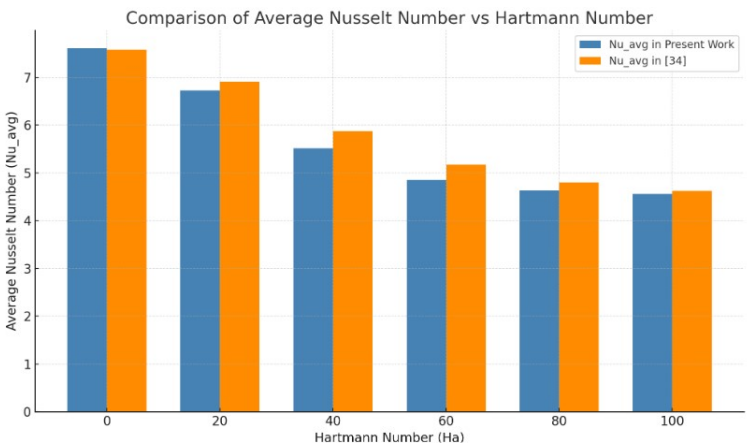

Fig. 6. Comparison of average Nusselt number Nu_{Avg} against (Ha).

7. Description of outcomes

The study concerns the thermophysical behavior of a TiO_2-H_2O nanoliquid in a triangular permeable enclosure using the finite element method (FEM) in COMSOL Multiphysics. The key parameters includethe Rayleigh number ($10^3 \leq Ra \leq 10^6$), Hartmann number ($0 \leq Ha \leq 100$), nanoparticle volume fraction ($0 \leq \phi \leq 0.05$), Darcy number ($10^{-5} \leq Da \leq 10^{-2}$), porosity ($0.2 \leq \epsilon \leq 0.6$), and Ree-Eyring ($0.1 \leq \lambda \leq 1$), $Pr = 7.0$ and ...=10∧-5 set constant. Results show the effects of these parameters on velocity and temperature distributions in terms of streamlines and isotherms, and global performance metrics such as local/average Nusselt numbers, total entropy generation, and Bejan number. This study shows the synergistic effect of MHD, Ree-Eyring's properties, and double-diffusive convection on heat and mass transfer for applications to energy-efficient systems such as solar stills.

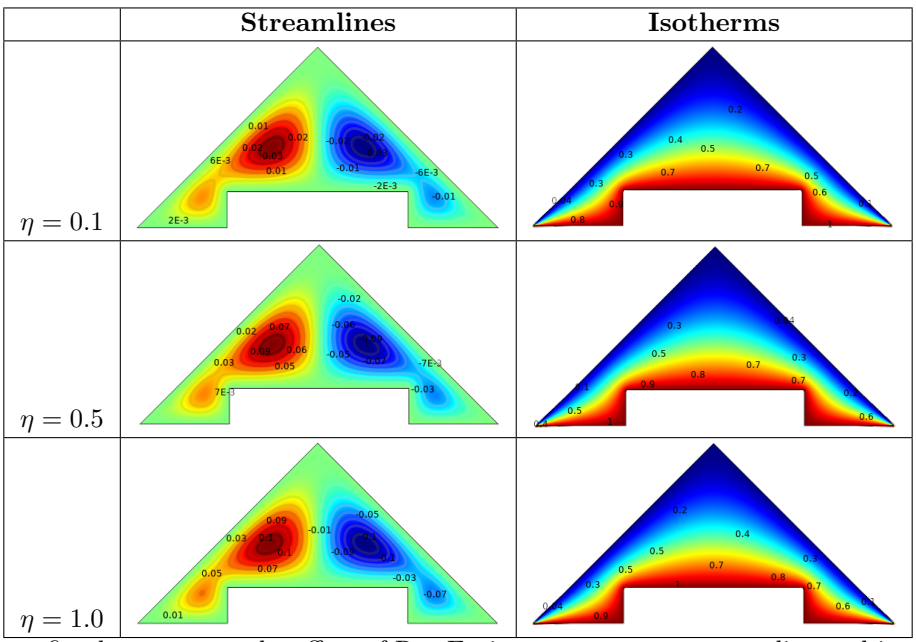

Fig. 7. Given fig, dememstrate the effect of Ree-Eyring parameter on streamline and isotherm line.

In Fig. **7.** The effects of the Ree-Eyring parameter (η) on the streamlines (left column) and the isotherms (right column) in a triangular cavity are described in the given figure. As we increase the Ree-Eyring parameters from ($\eta = 0.1$) to ($\eta = 1.0$), we see that the subsequent changes take place in the flow as well as the heat behavior. For streamlines, At low (η), e.g., at ($\eta = 0.1$), the flow circulation is weaker, indicated by the small streamline contours. In other words, it has lesser shear-thinning effects, which can make the fluid weak in building strong vortices. As (η) increases to 0.5 and 1.0, thus streamlines are showing a larger and denser vortex structure with circulation being more intense and higher. This happens due to the fact that this model of Ree-Eyring fluid is reducing at high values of (η) the effective viscosity and hence promotes stronger dynamics of flow. At isotherms, at ($\eta = 0.1$), one observes quite a uniform thermal gradient with the lines closer together in the heated area, signifying low convective heat transferral. As (η) goes from 0.5 to 1.0, the isotherms become more bent and distorted, which indicates the increase in convective heat transfer. Increasing (η) reduces the fluid resistance, strengthening the flow circulation and enhancing thermal convection. This indicates the importance of the Ree-Eyring parameter in controlling the interaction between shear-thinning effects and heat transfer processes in non-Newtonian fluids.

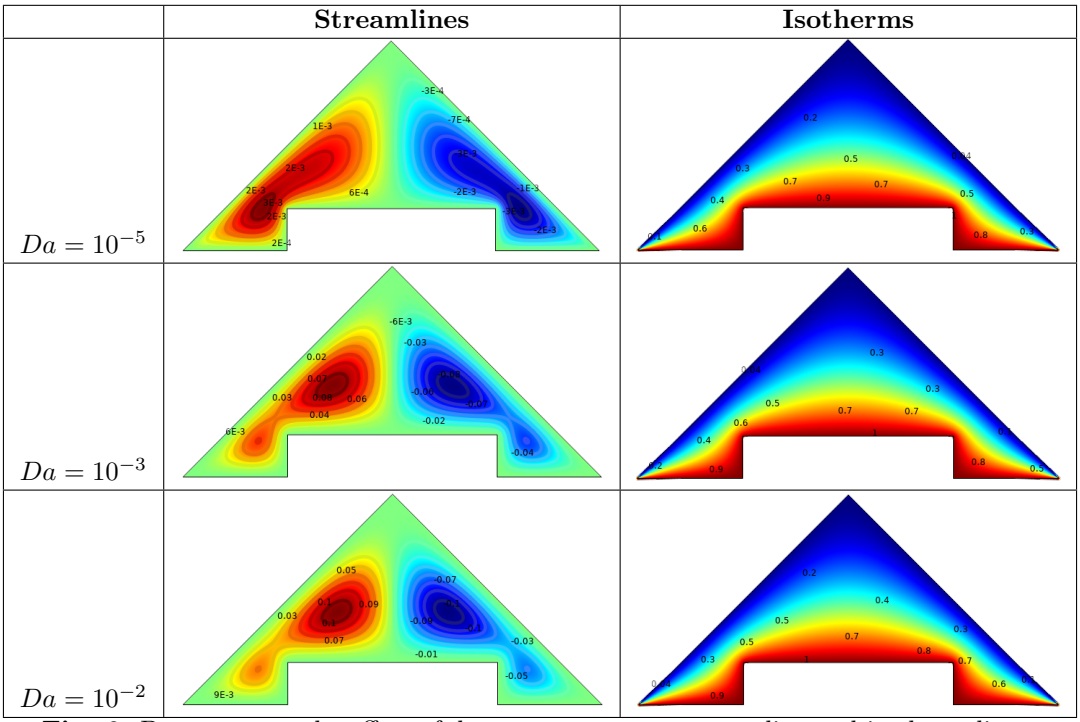

Fig. 8. Dememstrate the effect of darcy parameter on streamline and isotherm line.

In Fig. 8. The influence of the Darcy number (Da) on the streamlines (the left column) and on the isotherms (the right column) in a triangular enclosure is depicted in the given figure. This delineates the importance of their perviousness in the flow and heat transfer. Each row corresponds to a different value of ($Da = 10^{-5}$, 10^{-3}, and 10^{-2}). For streamlines, it showed that at (Da = 10^{-5}), where flow is highly restrained because of the porous medium's low-permeability medium. The streamlines are densely packed near the walls, containing weak circulations marked with values like ($1E-5$) and ($3E-5$). It indicates that viscous resistance is the controlling phenomena in restricting the fluid movement. Increasing permeability at (Da = 10^{-3}) causes a reduction in viscous resistance and subsequently allows further developing convective flow. There is evidence in the form of bigger vortices, with streamlines marked as (-0.03) and (0.04), meaning that more vigorous motion of fluid is present. The largest ever is (0.05) and (-0.05), whereby with sufficient permeability, high circulation is permitted throughout the domain. Beyond that, the flow is freed from furnace restrictions as convection shows dominance over resistance. For isotherms, it represented an almost conduction-type temperature distribution at (Da = 10^{-5}): nearly vertical isotherms at (0.3), (0.7), and (1.0). Heat transfer is dispersed primarily by thermal diffusion, moving fluid and low permeability, which restricts the motion of fluid. For (Da = 10^{-3}), there is slight beginning evidence of isotherms getting warmer on the inside and curving at both ends, including the (0.5) and (0.7) labels. This marks the conversion at which conduction-dominated isotherms are switching to mixed conduction-convection ones. Isotherms are much bent over into the tilted condition called with labels (0.5) and (1.0) at this (Da = 10^{-2}). They now clearly display the surface area for convection as superior to conduction. Consequently, the temperature gradients are disrupted by the strong flow patterns, enabling heat transfers across the entire domain.

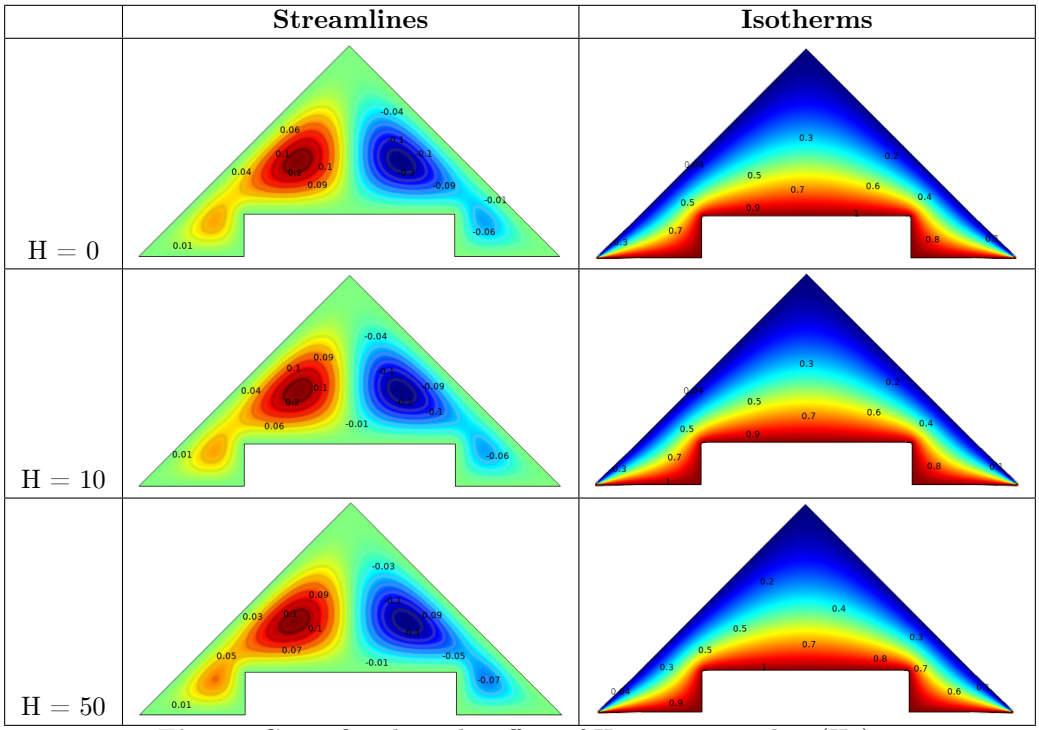

Fig. *9*. Given fig, show the effect of Hartmann number (Ha)

Fig. 9**,** demonstrates the effect of the Hartmann number (Ha) on the streamline and isotherm patterns. As the Hartmann number increases, the influence of the magnetic field on both the flow and temperature distribution becomes more significant. At H = 0, where the magnetic field is absent, the streamlines exhibit smooth, circular vortices, and the isotherms are evenly spaced (e.g., 0.1, 0.2, 0.4, 0.9), indicating uniform heat distribution. When H = 10 is applied, the magnetic field starts to restrict the flow, with the streamlines becoming more compact at the corners and the isotherms showing higher gradients (e.g., 0.9, 0.7), which suggests a reduction in heat transfer efficiency. At H = 50, the magnetic field significantly suppresses the flow, with streamlines nearly straight and parallel, particularly in the center. The isotherms are tightly curved, indicating a stronger thermal boundary layer and a further reduction in heat transfer. As Ha increases, the magnetic field restricts the flow and reduces heat transfer efficiency, as indicated by the changes in streamline labels (e.g., 0.1, -0.1, -0.04) and isotherm labels (e.g., 0.1, 0.2, 0.4, 0.9).

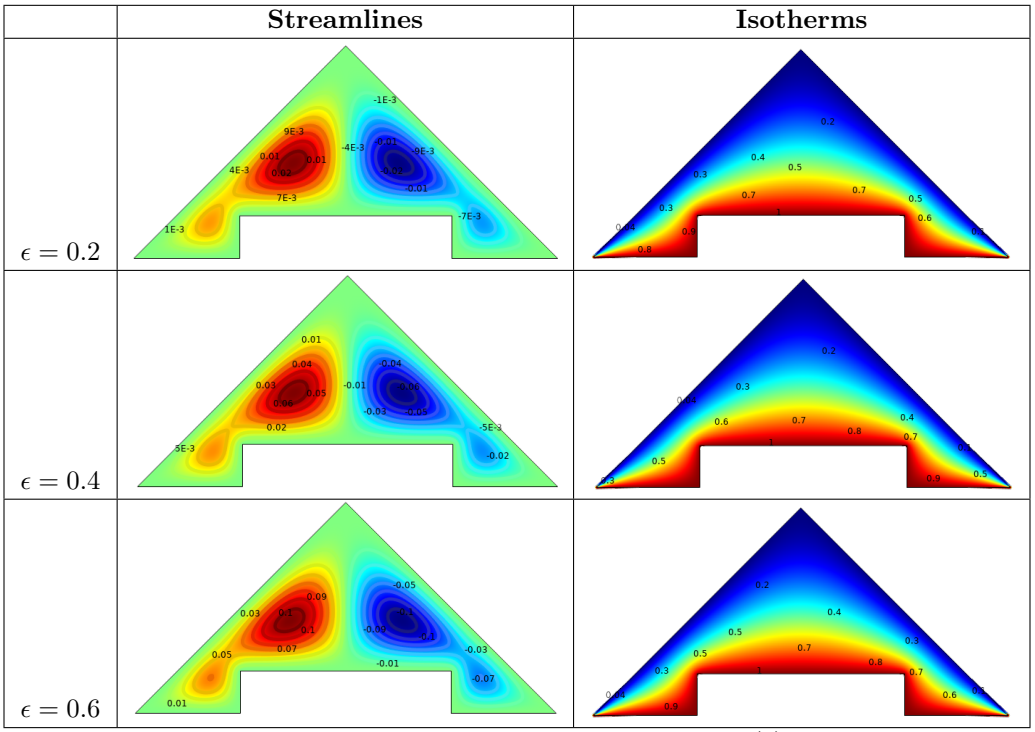

Fig. 10, show the effect of varying porosity (ε).

The Fig. 10**,** shows the effect of different porosities ($\epsilon = 0.2,\ 0.4,\ 0.6$) on streamlines and isotherms within a triangular cavity. The streamline counter at ($\epsilon = 0.2$) ranges from (-0.001) to (0.002), showing two weak vortices with low circulation due to higher flow resistance. The isotherm counter ranges from (0.2) to 1.0) with closely spaced isotherms near the heat source indicative of conduction-dominated heat transfer. At ($\epsilon = 0.4$) the streamline counter ranges from (-0.003) to (0.01) with stronger vortices due to reduced resistance while the isotherm counter remains (0.2) to (1.0) with increased distortion, depicting a balance between conduction and convection. Finally, at ($\epsilon = 0.6$) the streamline counter ranges from (-0.01) to (0.09), suggesting strong circulation with well developed vortices, while the isotherm counter spans the same range but indicates significant distortion and smoother gradients, typical of predominantly convective heat transfer. Thus, increased porosity promotes natural convection, increasing circulation strength and efficiency.

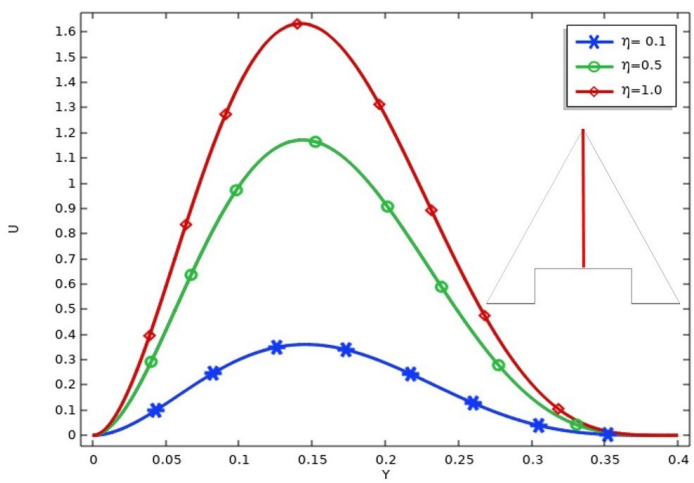

Fig. 11. Given fig, dememstrate the effect of Ree-Eyring parameter on streamline and isotherm line.

Fig. 11**,** depicts the horizontal velocity component (U) concerning the changes in Ree-Eyring within different parameter values of η. The more critical effector, therefore, as η keeps increasing, is the velocity profile elevation. This is so because as the Ree-Eyring increases, effective viscosity of the fluid decreases and, therefore, increases its flowability. In previous evidence, the resistance to motion decreases, and the effect on the fluid's motion becomes more pronounced toward speed increase. This behavior increases between the regions at higher shear rates. Nonlinear rheology properties of Ree-Eyring fluids exert a strong influence here on speed enhancement.

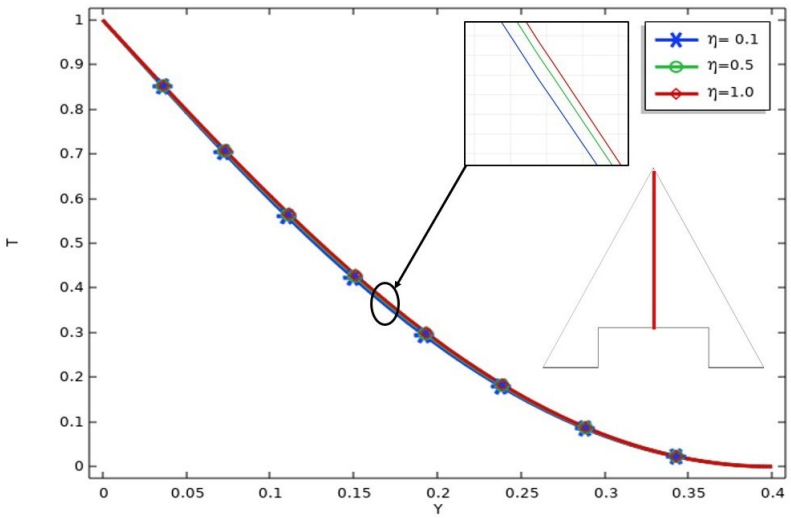

Fig. *12***.** Given fig, dememstrate the effect of Ree-Eyring parameter on streamline and isotherm line.

In Fig. 12**,** the graph depicts the effect of the Ree-Eyring parameter (η) on the temperature distribution in the cavity. At ($\eta = 0.1$), this temperature gradient appears to be much steeper as a result of the combined effects of convective heat transfer through strong shear-thinning effects, which facilitate the motion of fluids. As the value of eta increases to (0.5) and (1.0), the temperature profile becomes smoother, indicating reduced convection and the establishment of conduction as the dominant mode of heat transfer. This is because high eta diminishes the nonlinear rheological effects of the fluid, thereby limiting the ability of the fluid to carry heat through convection. The inset captures the most significant changes around ($y = 0.15$), where for larger values of eta, the temperature gradients are weaker.

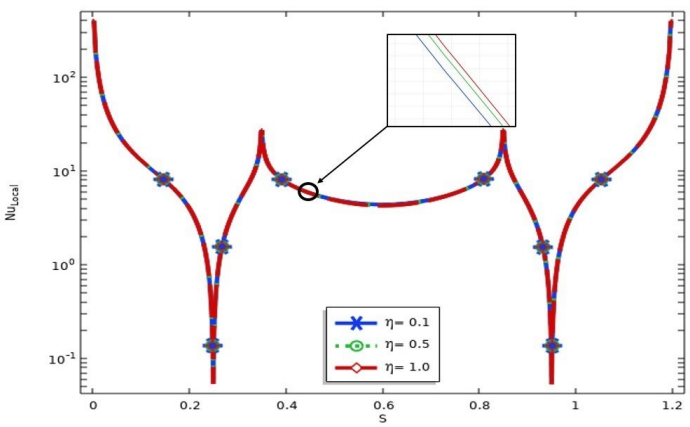

Fig. *13***.** Given fig, dememstrate the effect of Ree-Eyring parameter on streamline and isotherm line.

Fig. 13**,** It depicts the effect of Ree-Eyring parameter (η) on local Nusselt number (Nu_{local}) along the cavity surface. The graph reveals sharp peaks and valleys signifying regions of increased and diminished heat transfer in the local Nusselt number for all values of (η) (0.1, 0.5, and 1.0). Increasing (η) decreases

the insensitivity in the absolute profile towards the variations along the surface, i.e., it has lowered peak heights and smoother transitions at all levels. For lower values of (η) like ($\eta = 0.1$), strong shear-thinning effects increase convection, thus inducing higher local Nusselt number peaks in regions. As (η) is raised to (1.0), the behavioral pattern of the fluid transforms into a case of inducing weak effects of nonlinearity and consequently leads to a reduction in the ability to conduct convective heat transfer. The inset shows a very small region where curves denoted by different values of (η) of (Nu_{local}) deviate from one another, more around (s = 0.4). This implies that the more one increases (η), the more convection tends to suppression and heat transfer becomes uniform across the surface.

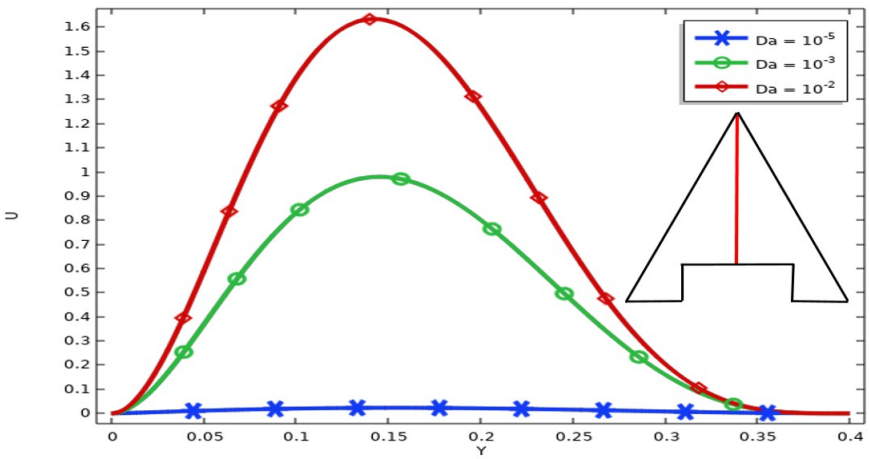

Fig. *14*. Given fig, dememstrate the effect of Darcy numbers (Da) on streamline and isotherm line.

The illustration Fig. 14**,** shows the way the horizontal velocity component (U) changes with increasing Darcy numbers (Da). As Da increases, the velocity profile shows a fairly steep increase. This is because higher values of Darcy number represent highly permeable porous medium, therefore offering reduced resistance to fluid flow. In other words, higher Da values allow for more fluid movement through the porous structure with minimal hindrance, thus enhancing the velocity within the system. Enhanced permeability offers better accessible fluid mobility and momentum transfers, thus elevates the velocity profile.

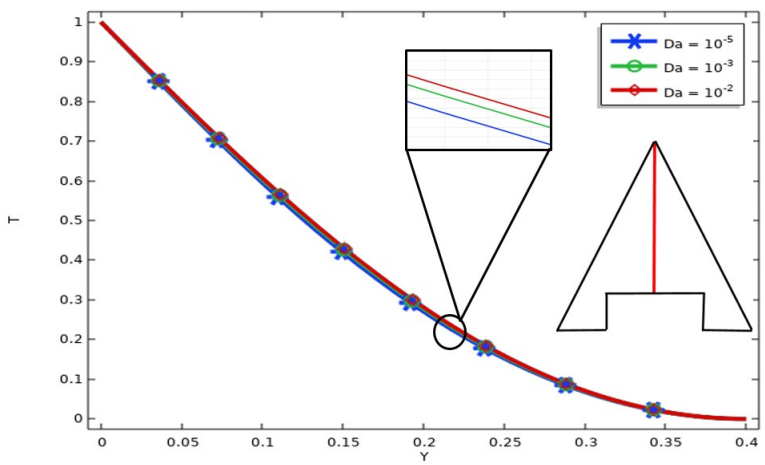

Fig. *15*. Given fig, dememstrate the effect of Darcy numbers (Da) on streamline and isotherm line.

The temperature's behavior with respect to the Darcy number (Da) is clearly shown in the Fig. 15. With increasing Darcy number from (10^{-5}) to (10^{-2}), the temperature profile flattens-in other words, the heat is well transferred by convection. An increase in Darcy number indicates to increase permeability of the porous medium and lets fluid travel faster, increasing convective heat transfer and decreasing thermal gradients in the system. For lower Darcy numbers such as (10^{-5}), the porous medium restricts

motion of the fluid, being an effect of conduction-dominated heat transfer. This gives rise to a more pronounced temperature gradient along the domain. For higher Darcy numbers such as (10^{-2}) however, convection complexity dominates, and that improved thermal mixing leads to more uniform temperature distribution. This trend is evident in the highlighted region especially, where the temperature drops more gradually as (Da) increases.

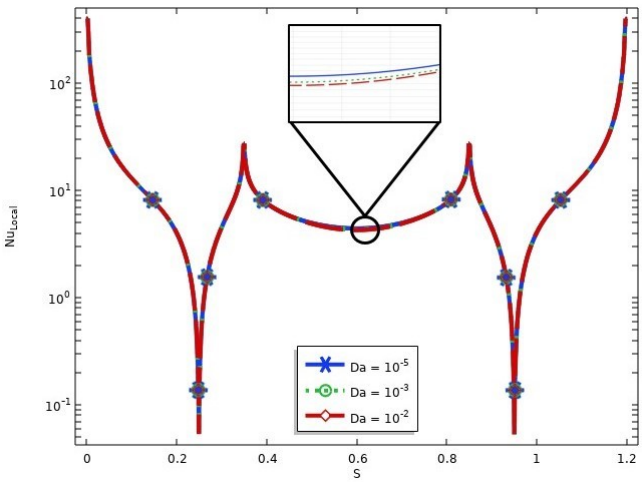

Fig. *16*. Given fig, dememstrate the effect of Darcy numbers (Da) on streamline and isotherm line.

Fig. 16**,** the graph portrays an impact of Darcy number on the local Nusselt number across the cavity surface. The increase of the local Nusselt number generally increases as the Darcy number increases; that is, as the Darcy number raises from the value of (10^{-5}) to (10^{-2}), the local Nusselt number increases in its peak regions. This is so because higher Darcy number indicates more porous medium, which is able to allow the fluid motion to be greater and increase the convective heat transfer. For lower Darcy numbers (10^{-5}), transmission has been restricted due to less permeability of the medium, discouraging the carrying away of heat by convection and, thus, reflected as lower (Nu_{local}) values.The inset represents a region within which differences in (Nu_{local}) become more prominent and highlighted for various Darcy numbers. High (Da) presents a greater convection effect and, hence, a steeper rise for heat transfer efficiency; on the contrary, lower (Da) heat transfer is more even and subdued distributed (Nu_{local}) because of their conduction-dominant. This behavior brings into line permeability in determining whether convection is predominant in porous media or conduction.

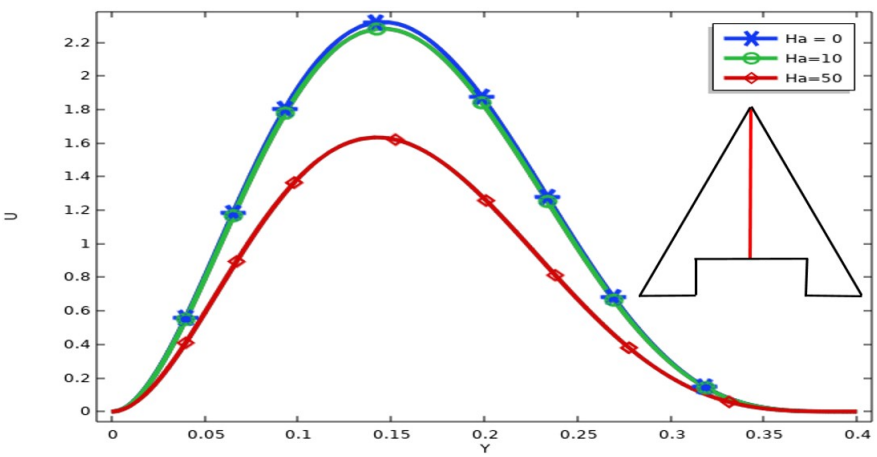

Fig. *17*. Given fig, dememstrate the effect of Hartmann Numbers (Ha) on streamline and isotherm line. The Fig. 17**,** depicts how the changes happen in the horizontal velocity component (U) corresponding to different Hartmann Numbers (Ha). As one progresses with higher Hartmann values, the velocity

magnitude decreases significantly. The main reason behind this is the development of Lorentz force that arises due to the magnetic field applied acting resistively against fluid motion. The stronger the magnetic field (or the higher the Ha), the stronger would be the suppression of momentum transport which leads to lowering the velocity. This interpretation would represent the effect of magnetic damping regarding the fluid flow becomes more restricted; therefore, inertial effects being suppressed would entrench a slower and more stabilized flow profile.

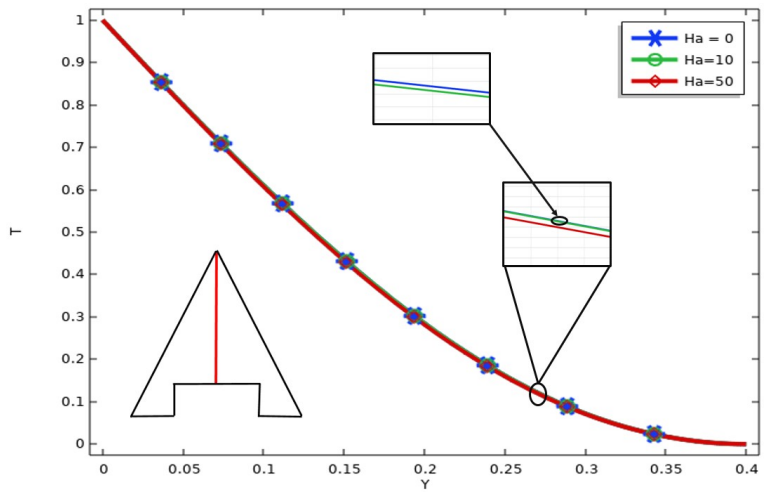

Fig. *18*. Given fig, dememstrate the effect of Hartmann Numbers (Ha) on streamline and isotherm line.

The Fig. 18**,** above depicts the influence of the Hartmann number (Ha) on the local Nusselt number. The local Nusselt number increases with higher values of Ha, as the presence of the magnetic field suppresses the motion of the fluid, thus reducing convective heat transfer and enhancing the relative contribution of conductive heat transfer. Physically, the Lorentz force dampens velocity gradients and stabilizes the temperature field, thereby introducing a higher temperature gradient at the walls, which leads to an increase in the Nusselt number. This has a greater contribution in regions where temperature differences are high.

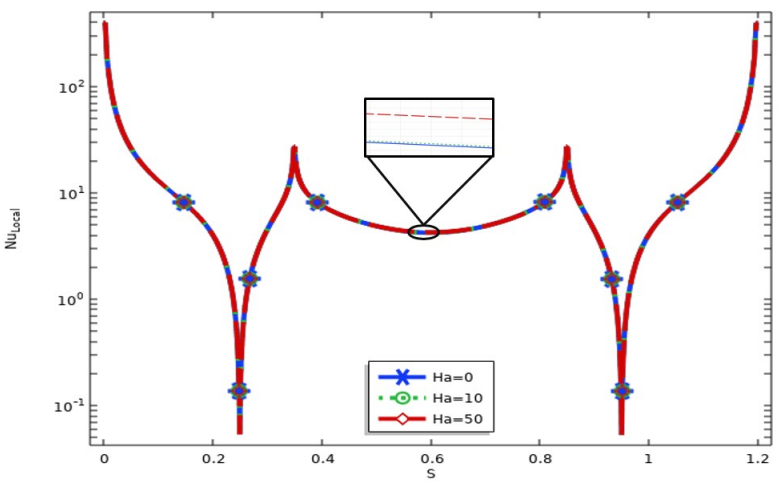

Fig. *19*. Given fig, dememstrate the effect of Hartmann Numbers (Ha) on streamline and isotherm line.

The Fig. 19**,** depicts the influence of the Hartmann number (Ha) on the local Nusselt number. The local Nusselt number increases with higher values of Ha, as the presence of the magnetic field suppresses the motion of the fluid, thus reducing convective heat transfer and enhancing the relative contribution of conductive heat transfer. Physically, the Lorentz force dampens velocity gradients and stabilizes the

temperature field, thereby introducing a higher temperature gradient at the walls, which leads to an increase in the Nusselt number. This has a greater contribution in regions where temperature differences are high.

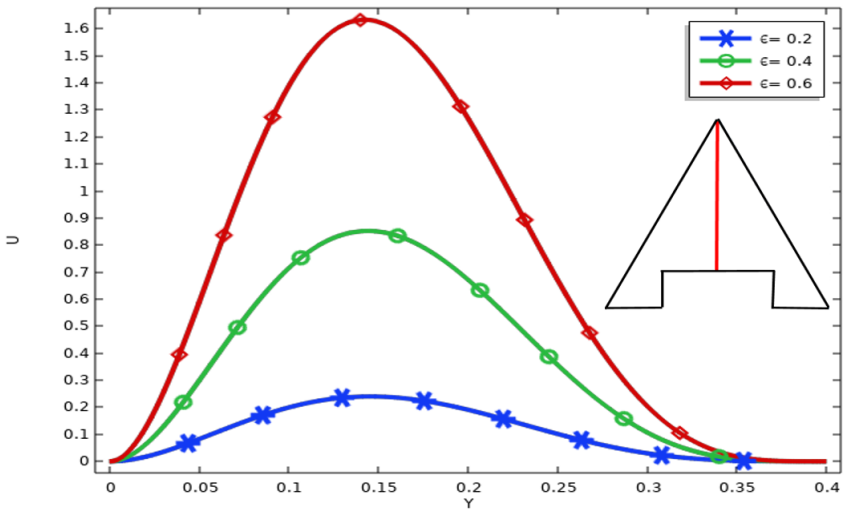

Fig. *20*, dememstrate the effect of porosity values (ϵ) on streamline and isotherm line.

Fig. 20, accompanies the text illustrates the comparisons of the horizontal velocity component (U) against varying porosity values (ϵ). As ϵ is made larger, the velocity profile also improves. This occurs because the greater the porosity, the less restrictive the porous medium becomes and allows the fluid to flow more freely as a consequence. This translates into physical terms as the decrease in flow resistance and increase in momentum transport with respect to the fact that flow has much fewer obstructions within the medium. Thus, the velocities increase in relation to the improved permeability and fluid mobility present in the system.

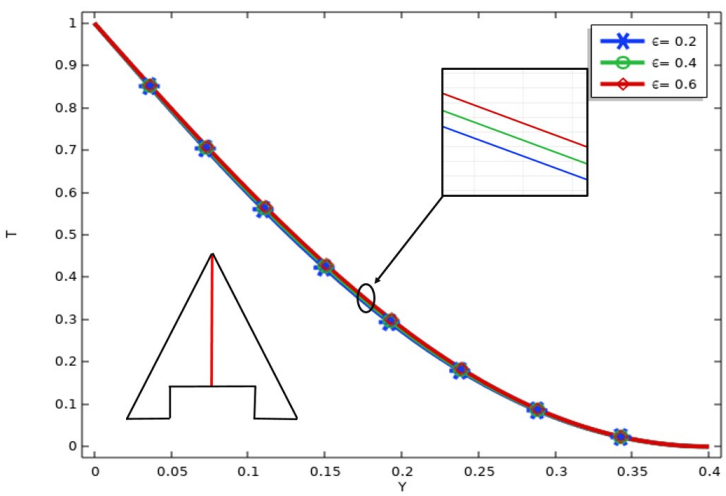

Fig. *21*, depicts the effect of porosity (ϵ) medium on temperature profile

Fig. 21, demonstrate the higher values of porosity (ϵ) of the medium increase temperature profile due to enhanced heat transport mechanism. Given that a porous medium with larger porosity offers less resistance to fluid movement, it can mix better with the solid matrix, enhance heat transfer between it and the fluid, and thus facilitate energy exchange between them more efficiently, raising the temperature distribution throughout the porous medium. Physically, less obstruction in the porous medium results in convective predominance over conductive and thus an increase in temperature.

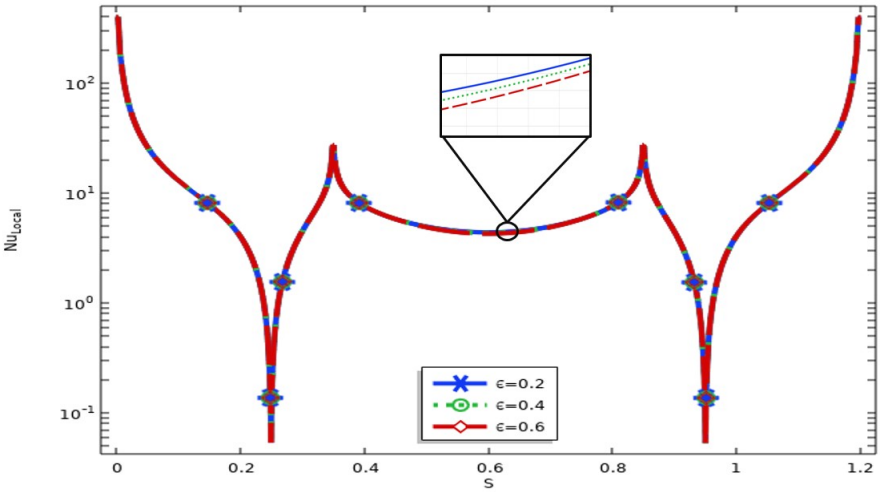

Fig. *22.* depicts the effect of porosity (ϵ) medium on Nusselt number.

The present Fig. 22**,** graph shows how porosity (ϵ) affects the local Nusselt number. With an increase in porosity, the local Nusselt number has a reduced value because of a decreased contribution of the solid matrix with respect to conduction to the heat transfer in a porous medium. As the porosity increase, the medium becomes less dense which again decreases the thermal conductivity of solid structure. This reduces heat transfer capabilities of the porous medium, particularly near the boundaries. Thus, the larger the porosity, convection dominates heat transfer, resulting in decreased heat flux at boundaries and therefore produces reduced local Nusselt numbers.

Table *4***.** Physical impacts of Ree-Eyring parameter (η) on entropies.

$\boldsymbol{\eta}$	$\boldsymbol{Nu_{Avg}}$	$\boldsymbol{Si_{Toatl}}$	$\boldsymbol{Be_{Avg}}$	$\boldsymbol{Si_{Vis}}$	$\boldsymbol{Si_{Th}}$	$\boldsymbol{Si_{Mg}}$
0.1	17.956	16.784	0.19999	0.0000013849	16.784	0.00010620
0.5	17.957	16.786	0.19993	0.000016707	16.785	0.0012048
1.0	17.957	16.788	0.19986	0.000035152	16.785	0.0024444

The table 4**,** presented here utilized the Ree-Eyring parameter (η). The average Nusselt number (Nu_{Avg}) has occurred, remaining almost not imperturbed though changes between 0.1 and 1.0 are recorded at an almost imperceptible percentage of (0.0056 %), practically pointing away that heat transfer is hardly affected by the Ree-Eyring parameter. The total entropy generation (Si_{Total}) grew just slightly by (0.0119 %), while the Bejan number (Be_{Avg}) marginally decreased by (0.07 %), hinting at slight shifting of balance in irreversibilities. The viscous entropy generation (Si_{Vis}) has jumped significantly upward by (60.5 %), indicating higher values of (η) magnifying the effects of viscous dissipation. The thermal entropy generation (Si_{Th}) is relatively constant, with an almost negligible increase of (0.00596 %). In contrast, the magnetic entropy generation (Si_{Mg}) has sharply increased to (95.6 %), showing that the forces of agnetism grow heavier as (η) increases. Ree-Eyring parameters thus majorly affect entropy generation using viscous and magnetic effects. This means it does change in heat transfer.

Table *5***.** Physical impacts of Darcy number (Da) on entropies.

$\boldsymbol{Da}$	$\boldsymbol{Nu_{Avg}}$	$\boldsymbol{Si_{Toatl}}$	$\boldsymbol{Be_{Avg}}$	$\boldsymbol{Si_{Vis}}$	$\boldsymbol{Si_{Th}}$	$\boldsymbol{Si_{Mg}}$
10^{-5}	17.956	16.784	0.20000	0.0000000025268	16.784	0.0000024026
10^{-3}	17.957	16.786	0.19994	0.0000031733	16.784	0.0011982
10^{-2}	17.957	16.788	0.19986	0.000035152	16.785	0.0024444

The table 5, above exhibits the influence of Darcy number (Da) to heat and entropy generation parameters. The average Nusselt number (Nu_{Avg}) is kept nearly constant with a minor percentage of (0.0056%) as the Darcy number varies from (10^{-5}) to (10^{-2}), indicating a little effect on heat transfer. SI total increased slightly by (0.0119%), while Be reduced to (0.07%), indicating slight reduction in heat transfer irreversibility dominance. Almost all viscous entropy generation increased by (99.2%), signifying that permeability increases viscous dissipation. Thermal entropy (Si_{Th}) generation increased marginally by (0.00596 %,) while the magnetic entropy generation term rises sharply by (99.2%) indicating that as permeability increases, the influence of magnetic effects increases sharply. These results suggest that at

higher (Da), the performance of viscous and magnetic dissipation increases while heat transfer remains largely unaffected.

Table 6. Physical impacts of Hartmann number (Ha) on entropies.

Ha	Nu_{Avg}	Si_{Toatl}	Be_{Avg}	Si_{Vis}	Si_{Th}	Si_{Mg}
0	17.958	16.786	0.20000	0.000047334	16.786	0.0000
10	17.958	16.786	0.19999	0.000046641	16.786	0.00015497
50	17.957	16.788	0.19986	0.000035152	16.785	0.0024444

The effect of Hartmann number (Ha) on heat transfer and entropy generation parameters is shown in the table 6. Average Nusselt number (Nu_{Avg}) shows an insignificant reduction of only (0.00557 %), total entropy generation (Si_{Total}) has increased slightly by only (0.0119 %). This indicates that magnetic fields have very little effect on total heat transfer and the generation of entropy. The Bejan number (Be_{Avg}) decreases slightly, with an overall change of only (0.07 %), indicating a minor reduction in the dominance of heat transfer irreversibility over other forms of entropy generation. The most relevant effect was noticed in viscous entropy generation (Si_{Vis}),which turns out to be reduced by (25.77 %), indicating that the magnetic field inhibits the movement of fluids, thus reducing viscous dissipation. On the other hand, the magnetic entropy generation, (Si_{Mg}), rises abruptly by (100 %); this shows that magnetic field becomes the real and dominant source of entropy generation at higher (Ha). This observation reveals that though the magnetic field diminishes viscous effects into all others, it generates some additional irreversibility that is imposed by the magnetic forces.

Table 7. Physical impacts of porosity parameter (ϵ) on entropies.

ϵ	Nu_{Avg}	Si_{Toatl}	Be_{Avg}	Si_{Vis}	Si_{Th}	Si_{Mg}
0.2	17.956	16.784	0.20000	0.00000056186	16.784	0.000044836
0.4	17.957	16.785	0.19996	0.0000080470	16.784	0.00060532
0.6	17.957	16.788	0.19986	0.000035152	16.785	0.0024444

Table 7, reveals the influence of porosity parameter (ϵ) on heat transfer and entropy gen eration parameter. From this, it can be inferred that the average Nusselt number (Nu_{Avg}) changed negligibly, with a percentage change of just 0.0056%, indicating that porosity affects heat transfer rates very minimally. The total entropy generation increased by 0.0119%, and the Bejan number showed a slight decrease of 0.07%, which indicates a little reduction in heat transfer irreversibility predominance. The viscous entropy contribution showed a significant increase by 84.1%. This infers that the viscous dissipation has greater increase with increasing porosity. Near constant change with a negligible increase of only 0.00596% for thermal entropy generation was reported. However, magnetic entropy generation reported a steep rise of 81.7%, which shows the magnetic effects become more pronounced at higher levels of porosity. These results indicated considerable influence of increased porosity on viscous and magnetic dissipation with little change in overall heat transfer and thermal entropy generation.

8. Conclusion

Our results indicate that desalination performance in thermally driven systems can be enhanced by parameter optimization. The parametric analysis reveals that the Ree-Eyring parameter (η) plays a decisive role in desalination-related thermal management by significantly enhancing fluid circulation through shear-thinning effects, thereby improving brine mixing and uniform heat distribution.Increasing the Ree-Eyring parameter improves flow ability and temperature uniformity, supporting efficient brine heating. Higher Darcy numbers increase permeability and convective transport, maximizing thermal energy use and boosting evaporation rates. Porosity adjustments can improve mixing and temperature distribution, though optimal values must be chosen to avoid reduced local heat transfer efficiency. The Hartmann number offers a tool for magnetic flow control but should be limited to avoid excessive suppression of convection. Overall, the interplay between η, Da, Ha, and ϵ determines the balance between heat delivery and energy loss, and our study provides a framework for tuning these parameters to improve the thermal efficiency and freshwater yield of desalination systems.

Applications and Future Directions

The Ree-Eyring parameter has become central to the development of new advanced lubricants, so as to biomedical devices or energy storage systems in which highly controlled non-Newtonian fluid behavior and heat transfer are desired characteristics. Optimizing the Darcy number serves to enhance geothermal energy extraction, improve porous insulation materials, as well as filtration systems by achieving an optimum balance in conduction and convection. The Hartmann number has thus been a concern over magnetohydrodynamic generators, cooling systems in nuclear reactors, as well as plasma flow control in space propulsion. Moreover, improved porosity brings about enhanced efficiency in heat exchangers, packed bed reactors, and thermal energy storage units through the promotion of stronger convection along with enhanced heat transfer. Future research directions will involve hybrid fluid systems incorporating Ree-Eyring properties within porous media for enhanced thermal applications, designing adaptive smart materials, and magnetic field-based influences in energy-efficient renewables and space technologies. Exploration altogether of entropy management strategies will yield dividends for the cause of future sustainable and efficient thermal systems.

Data availability

The datasets used and/or analyzed during the current study are available from the corresponding author upon reasonable request.

Author's contributions

All authors participated equally in the conceptualization, investigation, analysis, original draught Writing, review, and editing of the work.

Declarations

Ethics Approval and Consent to Participate Not applicable.

Consent for Publication Not applicable.

Competing Interests We declare that we do not have any commercial or associative interest that represents a conflict of interest in connection with the work submitted.

References

1. Ghachem, K., Kolsi, L., Mâatki, C., Hussein, A.K., Borjini, M.N., *Numerical simulation of three-dimensional double diffusive free convection flow and irreversibility studies in a solar distiller*, Int. Commun. Heat Mass Transf. 39, 869–876, (2012).
2. Ghachem, K., Ben Hamida, M.B., Maatki, C., Kolsi, L., Borjini, M.N., Ben Aissia, H., *Numerical study of combined natural convection and radiation in three dimensional solar thermal collector: focus on the inclination effect on heat transfer*, Am. J. Mod. Energy 1, 44–51, (2015).
3. Ghachem, K., Maatki, C., Kolsi, L., Alshammari, N., Oztop, H.F., Borjini, M.N., Ben, A.H., Al-Salem, K., *Numerical study of heat and mass transfer optimization in a 3D inclined solar distiller*, Therm. Sci. 21, 2469–2480, (2017).
4. Dhiman, N.K., *Transient analysis of a spherical solar still*, Desalination 69, 47–55, (1988).
5. Kabeel, A.E., *Performance of solar still with a concave wick evaporation surface*, Energy 34, 1504–1509, (2009).
6. Ismail, B.I., *Design and performance of a transportable hemispherical solar still*, Renew. Energy 34, 145–150, (2009).
7. Arunkumar, T., Jayaprakash, R., Denkenberger, D., Ahsan, A., Okundamiya, M.S., Tanaka, H., Aybar, H., others, *An experimental study on a hemispherical solar still*, Desalination 286, 342–348, (2012).
8. Gorjian, S., Ghobadian, B., Hashjin, T.T., Banakar, A., *Experimental performance evaluation of a stand-alone point-focus parabolic solar still*, Desalination 352, 1–17, (2014).
9. Tiwari, G.N., Kumar, A., *Nocturnal water production by tubular solar stills using waste heat to preheat brine*, Desalination 69, 309–318, (1988).
10. Ahsan, A., Imteaz, M., Rahman, A., Yusuf, B., Fukuhara, T., *Design, fabrication and performance analysis of an improved solar still*, Desalination 292, 105–112, (2012).
11. Elashmawy, M., *An experimental investigation of a parabolic concentrator solar tracking system integrated with a tubular solar still*, Desalination 411, 1–8, (2017).
12. Taamneh, Y., Taamneh, M.M., *Performance of pyramid-shaped solar still: Experimental study*, Desalination 291, 65–68, (2012).
13. Fath, H.E.S., El-Samanoudy, M., Fahmy, K., Hassabou, A., *Thermal-economic analysis and comparison between pyramid-shaped and single-slope solar still configurations*, Desalination 159, 69–79, (2003).
14. Kianifar, A., Heris, S.Z., Mahian, O., *Exergy and economic analysis of a pyramid-shaped solar water purification system: active and passive cases*, Energy 38, 31–36, (2012).

15. Arunkumar, T., Jayaprakash, R., Prakash, A., Suneesh, P.U., Karthik, M., Kumar, S., *Study of thermophysical properties and an improvement in production of distillate yield in pyramid solar still with boosting mirror*, Indian J. Sci. Technol. 3, 879–884, (2010).

16. Kabeel, A.E., El-Maghlany, W.M., Abdelgaied, M., Abdel-Aziz, M.M., *Performance enhancement of pyramid-shaped solar stills using hollow circular fins and phase change materials*, J. Energy Storage 31, 101610, (2020).

17. Ravishankara, S., Nagarajan, P.K., Vijayakumar, D., Jawahar, M.K., *Phase change material on augmentation of fresh water production using pyramid solar still*, Int. J. Renew. Energy Dev. 2, 115–120, (2013).

18. Sathyamurthy, R., Kennady, H.J., Nagarajan, P.K., Ahsan, A., *Factors affecting the performance of triangular pyramid solar still*, Desalination 344, 383–390, (2014).

19. Nagarajan, P.K., El-Agouz, S.A., Arunkumar, T., Sathyamurthy, R., *Effect of forced cover cooling technique on a triangular pyramid solar still*, Int. J. Ambient Energy 38, 597–604, (2017).

20. Sathyamurthy, R., Nagarajan, P.K., Kennady, H., Ravikumar, T.S., Paulson, V., Ahsan, A., *Enhancing the heat transfer of triangular pyramid solar still using phase change material as storage material*, Front. Heat Mass Transf. 5, (2014).

21. Naveen Kumar, P., Harris Samuel, D.G., Nagarajan, P.K., Sathyamurthy, R., *Theoretical analysis of a triangular pyramid solar still integrated to an inclined solar still with baffles*, Int. J. Ambient Energy 38, 694–700, (2017).

22. Almeshaal, M.A., Maatki, C., Kolsi, L., Ghachem, K., Chamkha, A., *3D Rayleigh-Bénard-type natural convection in MWCNT-nanofluid-filled L-shaped enclosures with consideration of aggregation effect*, Math. Methods Appl. Sci., (2020).

23. Hussain, S., Jamal, M., Maatki, C., Ghachem, K., Kolsi, L., *MHD mixed convection of Al_2O_3–Cu–water hybrid nanofluid in a wavy channel with incorporated fixed cylinder*, J. Therm. Anal. Calorim. 144, 2219–2233, (2021).

24. Hadji, L., Meziane, M.A.A., Safa, A., *A new quasi-3D higher shear deformation theory for vibration of functionally graded carbon nanotube-reinforced composite beams resting on elastic foundation*, Struct. Eng. Mech. 66, 771–781, (2018).

25. Hadji, L., Avcar, M., Civalek, Ö., *An analytical solution for the free vibration of FG nanoplates*, J. Brazilian Soc. Mech. Sci. Eng. 43, 418, (2021).

26. Hadji, L., Avcar, M., *Nonlocal free vibration analysis of porous FG nanobeams using hyperbolic shear deformation beam theory*, Adv. Nano Res. 10, 281–293, (2021).

27. Khelifa, Z., Hadji, L., Daouadji, T.H., Bourada, M., *Buckling response with stretching effect of carbon nanotube-reinforced composite beams resting on elastic foundation*, Struct. Eng. Mech. 67, 125–130, (2018).

28. Farbod, M., Ahangarpour, A., Etemad, S.G., *Stability and thermal conductivity of water-based carbon nanotube nanofluids*, Particuology 22, 59–65, (2015).

29. Kabeel, A.E., Omara, Z.M., Essa, F.A., *Numerical investigation of modified solar still using nanofluids and external condenser*, J. Taiwan Inst. Chem. Eng. 75, 77–86, (2017).

30. Sharshir, S.W., Peng, G., Wu, L., Yang, N., Essa, F.A., Elsheikh, A.H., Mohamed, S.I.T., Kabeel, A.E., *Enhancing the solar still performance using nanofluids and glass cover cooling: experimental study*, Appl. Therm. Eng. 113, 684–693, (2017).

31. Kabeel, A.E., Sathyamurthy, R., Sharshir, S.W., Muthumanokar, A., Panchal, H., Prakash, N., Prasad, C., Nandakumar, S., El Kady, M.S., *Effect of water depth on a novel absorber plate of pyramid solar still coated with TiO_2 nano black paint*, J. Clean. Prod. 213, 185–191, (2019).

32. Al-Rashed, A., Kolsi, L., Kalidasan, K., Maatki, C., Borjini, M., Aichouni, M., Kanna, P.R., *Effect of magnetic field inclination on magneto-convective induced irreversibilities in a CNT–water nanofluid filled cubic cavity*, Front. Heat Mass Transf. 8, 31, (2017).

33. Xue, Q.Z., *Model for the effective thermal conductivity of carbon nanotube composites*, Nanotechnology 17, 1655, (2006).

34. Rahman, M.M., Oztop, H.F., Ahsan, A., Kalam, M.A., Varol, Y., *Double-diffusive natural convection in a triangular solar collector*, Int. Commun. Heat Mass Transf. 39, 264–269, (2012).

35. Radouane, F., Abderrahmane, A., Mebarek-Oudina, F., Ahmed, W., Rashad, A.M., Sahnoun, M., Ali, H.M., *Magneto-free convection of hybrid nanofluid inside non-darcy porous enclosure containing an adiabatic rotating cylinder*, Energy Sources, Part A Recover. Util. Environ. Eff., 1–16, (2020).

36. Esfe, M.H., Arani, A.A.A., Rezaie, M., Yan, W.-M., Karimipour, A., *Experimental determination of thermal conductivity and dynamic viscosity of Ag–MgO/water hybrid nanofluid*, Int. Commun. Heat Mass Transf. 66, 189–195, (2015).

37. Mahian, O., Kolsi, L., Amani, M., Estellé, P., Ahmadi, G., Kleinstreuer, C., Marshall, J.S., Siavashi, M., Taylor, R.A., Niazmand, H., *Recent advances in modeling and simulation of nanofluid flows-Part I: Fundamentals and theory*, Phys. Rep. 790, 1–48, (2019).

38. Woods, L.C., *The thermodynamics of fluid systems*, Oxford, (1975).

39. Mahmoodi, M., *Numerical simulation of free convection of a nanofluid in L-shaped cavities*, Int. J. Therm. Sci. 50, 1731–1740, (2011).

40. Maxwell, J.C., *A treatise on electricity and magnetism*, Clarendon Press, (1873).

41. Hamilton, R.L., Crosser, O.K., *Thermal conductivity of heterogeneous two-component systems*, Ind. Eng. Chem. Fundam. 1, 187–191, (1962).

42. Einstein, A., *A new determination of molecular dimensions*, Annln. Phys. 19, 289–306, (1906).

43. Basak, T., Roy, S., Balakrishnan, A.R., *Effects of thermal boundary conditions on natural convection flows within a square cavity*, Int. J. Heat Mass Transf. 49, 4525–4535, (2006).

44. Dutta, S., Pati, S., Baranyi, L., *Numerical analysis of magnetohydrodynamic natural convection in a nanofluid filled quadrantal enclosure*, Case Stud. Therm. Eng. 28, 101507, (2021).

Hamayat Ullah,
Department of Mathematical Sciences,
University of Lakki Marwat, Lakki Marwat 28420, KPK, Pakistan.
E-mail address: hamayatullahmath17@gmail.com

and

Muhammad Salim Khan,
Department of Mathematical Sciences,
University of Lakki Marwat, Lakki Marwat 28420, KPK, Pakistan.
E-mail address: salimgul.433@gmail.com

and

Zahir Shah,
Department of Mathematical Sciences,
University of Lakki Marwat, Lakki Marwat 28420, KPK, Pakistan.
E-mail address: zahir@ulm.edu.pk

and

Aseel Smerat,
Faculty of Educational Sciences,
Al-Ahliyya Amman University, Amman, 19328, Jordan.
Department of Biosciences, Saveetha School of Engineering,
Saveetha Institute of Medical and Technical Sciences, Chennai, 602105, India.
E-mail address: smerat.2020@gmail.com

and

Maria Alina Fălădău,
Faculty of Engineering,
Lucian Blaga University of Sibiu, 550024 Sibiu, Romania.
E-mail address: alina.gligor@ulbsibiu.ro